Acoustic response of structured and randomized porous blunt trailing edges subject to turbulent boundary layers

Arcondoulis, Elias J.G.; Ragni, Daniele; Fiscaletti, Daniele; Merino-Martinez, Roberto; Liu, Yu

DOI
10.1121/10.0028189

Publication date
2024

Document Version
Final published version

Published in
Journal of the Acoustical Society of America

AUGUST 13 2024

Acoustic response of structured and randomized porous blunt trailing edges subject to turbulent boundary layers

Elias J. G. Arcondoulis ; Daniele Ragni ; Daniele Fiscaletti; Roberto Merino-Martinez ; Yu Liu

J. Acoust. Soc. Am. 156, 1029–1040 (2024)
https://doi.org/10.1121/10.0028189

JASA ARTICLE

Acoustic response of structured and randomized porous blunt trailing edges subject to turbulent boundary layers

Elias J. G. Arcondoulis,[1,a)] Daniele Ragni,[2,b)] Daniele Fiscaletti,[3] Roberto Merino-Martinez,[2] and Yu Liu[4]

[1]*School of Civil Aerospace and Design Engineering, University Walk, Bristol BS8 1TR, United Kingdom*

[2]*Faculty of Aerospace Engineering, Kluyverweg 1, 2629HS Delft, The Netherlands*

[3]*Faculty of Mechanical Engineering, Mekelweg 2628CD, Delft, The Netherlands*

[4]*Southern University of Science and Technology, Shenzhen, Guangdong, 518055, People's Republic of China*

ABSTRACT:

The attachment of porous media to a blunt trailing edge (TE) can significantly suppress vortex shedding processes and the related tonal noise, yet the near-wall and internal flow fields of porous media are difficult to analyze experimentally and rely on numerical simulations to elucidate the internal flow features. A structured porous trailing edge (SPTE) has been recently designed that follows a methodology of a structured porous coated cylinder. The SPTE acoustic response was compared against randomized porous media with 10 and 30 pores/in. in an anechoic wind tunnel over a range of flow velocities. Acoustic beamforming revealed that the dominant acoustic sources were at the end of the solid plate, even when a porous TE was attached. A region of integration was used to extract acoustic spectra without additional noise sources, revealing that the SPTE possesses superior noise reduction capability. Dipolar directivity patterns were observed at the vortex shedding frequency for each TE, and the coherence between microphones revealed the complex acoustic propagation of the high-frequency content. A wavelet analysis revealed how the SPTE breaks periodic vortex shedding cycles into smaller cycles over a wider frequency range, leading to an overall noise reduction relative to the other TEs.

https://doi.org/10.1121/10.0028189

(Received 15 December 2023; revised 15 June 2024; accepted 22 July 2024; published online 13 August 2024)

[Editor: Xun Huang] Pages: 1029–1040

I. INTRODUCTION

Airfoil trailing edge (TE) noise is problematic for the design of on- and offshore wind turbines, aircraft, urban air mobility vehicles, and unmanned-aerial-vehicle transportation. The fundamental noise-generating mechanisms of turbulent boundary layer (TBL) broadband noise[1] and tonal noise[2] have been investigated for many years. A deeper understanding of these noise-generating mechanisms has led to the development of TE appendages, such as sharp-edged serrations[3–6] to suppress vortex shedding processes and acoustic pressure radiation. The study of blunt TEs, however, has been of a lesser focus, yet the rapid emergence of large wind turbines in recent years gives it greater relevance.[7] A significant portion of a large wind turbine blade possesses a blunt TE, which presents a unique challenge separate from typical sharp airfoil TEs and introduces bluff body flow dynamics. The blunt TE generates vortex shedding tonal noise with a characteristic frequency linked to the width of the TE[8] and increases the overall drag relative to a sharp TE.[9] To alleviate these vortex shedding processes, some active control methods have been proposed, including using plasma actuators to control the wake of a blunt TE[10] and blowing air through the blunt TE;[11] yet, these require energy input and are quite complicated to operate.

Porous TEs have been utilized more recently to minimize TBL TE noise, where a portion of the sharp TE is replaced with open-cell porous media.[12–14] The origin of using porous media to reduce airfoil noise during flight originated from Graham,[15] who observed the silent flight of owls and aimed to modify wing designs to mimic the owl wing. A fully porous airfoil was investigated by Geyer *et al.*,[16] who were able to show significant noise reductions, as compared to a solid baseline airfoil, yet at a compromise of a large increase in drag and loss of lift. Following this study, Geyer and Sarradj[13] used the same porous media only at the TE for lengths greater than 5% of the chord and reported much lower increases in drag and up to 8 dB noise reduction. Rubio Carpio *et al.*[14] conducted an experimental aeroacoustic study of a NACA 0018 airfoil with solid and porous TE inserts covering 20% of the chord length and observed low-frequency noise reduction of up to 11 dB. Similarly, Teruna *et al.*[17] replaced the last 20% of a NACA 0018 airfoil chord using a numerical porous model and revealed significant noise reduction (relative to a solid TE) and explained this due to reduced scattering intensity at the TE and a breakdown of spanwise coherence. They were able to reveal that the flow communication between the shear layers on the upper and lower surfaces of the porous TE played a significant role

[a)]Current address: University of Bristol, Bristol BS8 1TR, UK.
[b)]Email: D.Ragni@tudelft.nl

in the reduced scattering intensity. Recent simulations of a structured porous TE by Jiang *et al.*[18] also investigated the flow communication through the TE and revealed that low-frequency TE noise could be reduced, yet at the compromise of some additional high-frequency noise.

A collation of porous airfoil TE studies is presented in Fig. 1, as denoted by the filled symbols. The x axis, l/h, is the length of the exposed porous appendage, l (excluding any insert length not interacting with the flow), divided by its thickness, h (maximum thickness in the case of tapered/airfoil TEs), whereas the y axis corresponds to the Reynolds number based on l, i.e., $Re_l = U_0 l/\nu$. Typically, most airfoil porous TEs are investigated within $Re_l = 10^4$ to 10^5, yet the l/h-values can vary significantly; for example, Geyer and Sarradj[19] studied experimentally an SD7003 shape-airfoil with a very slender tapering TE, so that a small percent chord porous TE replacement had a large l/h-value. Nonetheless, typically most studies have replaced 20% or less of the airfoil chord to observe significant broadband noise reduction relative to a solid TE.

More recently, porous TEs have been appended to the blunt TE[7,22] using open-cell randomized porous media; the porous blunt TE studies investigated to date are presented in Fig. 1 as open symbols. The l/h-values studied are typically lower than the airfoil porous TEs (due to the airfoil porous TEs possessing a taper), where the porous TE lengths are clustered about $l/h \approx 2$, yet the Reynolds numbers are similar. Showkat Ali *et al.*[7] revealed that the use of open-cell porous TEs appended to a blunt solid TE leads to the suppression of the fundamental vortex shedding tonal frequency. They also showed that using a varying-length porous TE, the internal flow field within the porous TE and the vortex shedding weakening in the near-wake region are related and linked with l/h and that there exists a minimum-needed l/h-value to obtain meaningful tonal noise suppression to allow some flow penetration between the upper and lower shear layers (consistent with the findings of Teruna *et al.*[17] for a sharp TE).

Unfortunately, the internal flow fields of randomized porous media can be difficult to analyze experimentally (although they have been investigated numerically[17,28]). To alleviate this problem we present a structured porous trailing edge (SPTE) (see Fig. 2). The design of this structured porous media follows a previous study by Arcondoulis *et al.*,[29] who designed a structured porous coated cylinder (SPCC) in order to investigate the fundamental flow mechanisms within the porous media of a typical open-cell porous coated cylinder that can yield an excellent passive flow and noise control capability.[30] This concept of self-repeating structures, for the purpose of passive flow and noise control, is becoming more widespread and accepted as a viable alternative to randomized porous open-cell media.[23,29,31–37] The SPCC possesses direct lines of sight along the radial and circumferential directions of the material, thereby allowing for direct numerical simulation and flow visualization,[31] and is easier to control the internal porous parameters, such as porosity, as compared to randomized porous media. Here, the SPTE can be visualized as unwrapping the porous media of the SPCC from the cylinder into a straight segment, such that along the spanwise and vertical directions there exist clear lines of sight. The SPTE, like the SPCC, can be customized for a specific porosity and number of pores per inch (PPI), which is otherwise difficult to achieve using randomized porous media, such as metal foams or porous polyurethane. Furthermore, the SPTE can be manufactured using transparent materials via three-dimensional (3D) printing, which allows for tomographic particle image velocimetry (PIV) experiments in water to obtain time-resolved internal flow fields (as conducted using an SPCC[31]) It should be noted that Liu *et al.*[23] also followed the SPCC methodology of Arcondoulis *et al.*[29] and designed several varying-porosity SPTEs that are similar to that presented in this study. Their SPTEs, with varying porosity along the spanwise direction, significantly reduced the vortex shedding tone of a solid blunt TE; yet, they did not conduct a comparison against any randomized open-cell porous media,

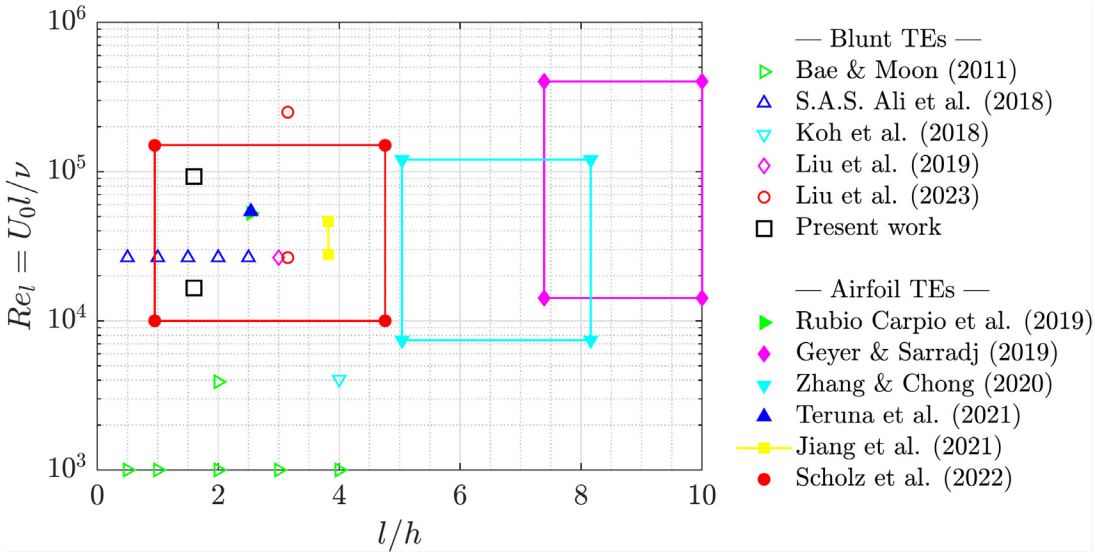

FIG. 1. (Color online) Collation of blunt porous TE (see Refs. 7 and 20–23) and airfoil porous TE (see Refs. 14, 19, and 24–27) studies, plotted in terms of the porous TE length-to-height ratio, l/h, and the Reynolds number calculated using the porous TE length, l, Re_l.

https://doi.org/10.1121/10.0028189

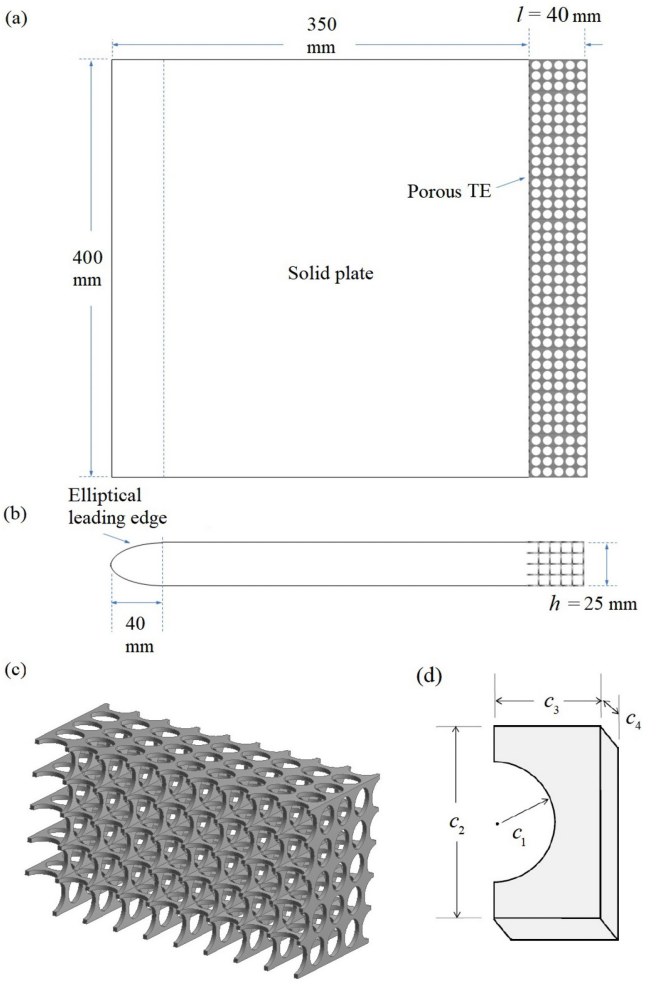

FIG. 2. (Color online) Schematic diagram of the SPTE attached to an elliptical-leading-edge plate. (a) Planform view, (b) side view, (c) portion of the SPTE geometry, and (d) C-chip used to create the porous media.

and it is, therefore, difficult to determine whether the noise reduction was due to structured porous media specifically or just due to any form of porous media (as observed by others[7]) for the same flow conditions. In addition, their SPTEs were designed with a length-to-height ratio of $l/h = 3.15$, which is approximately twice the ratio of the SPTE presented in this study and longer than those in most other blunt TE studies (refer to Fig. 1). It is therefore also difficult to determine from that study whether the SPTE is capable of passive flow and noise control capability with a significantly shorter length-to-height ratio,[7] or whether noise reduction is caused by the presence of a porous plate.[38]

This paper presents an experimental study of the aeroacoustic performance of both randomized and structured porous media (i.e., SPTE) appended to a solid TE of an elliptical-leading-edge flat plate. Experiments were conducted in an anechoic open-jet wind tunnel using an elliptical-leading-edge plate appended using three porous TEs: the SPTE and two randomized open-cell porous TEs with 10 and 30 PPI. These were all compared against the solid TE baseline (without any appendage). Acoustic beamforming, including acoustic pressure far-field measurements, was conducted at freestream flow velocities from 10 m/s to 35 m/s. The manuscript is organized as follows: The design of the SPTE and the methodology of the acoustic and flow-field experiments are discussed in Sec. II, Acoustic results including acoustic source maps, far-field acoustic spectra, directivity patterns, magnitude-squared coherence, and a wavelet analysis are presented and discussed in Sec. III, and a summary of the results is provided in Sec. IV.

II. METHODOLOGY

A. Wind tunnel

The experiments were conducted in the anechoic, vertical, open-jet wind tunnel (A-tunnel) at the Delft University of Technology (TU Delft).[39] The test section of the tunnel is located in an anechoic plenum composed of Flamex Basic acoustic absorbing foam wedges (Merford Noise Control B.V., Gorinchem, the Netherlands), resulting in a cut-off frequency of 200 Hz (i.e., free-field sound propagation conditions hold for higher frequencies). The nozzle employed in the A-tunnel has a contraction ratio of approximately 15:1 when equipped with a rectangular test section of 0.4 m $\times$ 0.7 m, resulting in a maximum flow velocity of 40 m/s. For the maximum flow velocity considered in this study (35 m/s), the streamwise turbulence intensity at the center of the nozzle's exit $(u'_{\mathrm{rms}}/U_0)|_{\mathrm{max}} < 0.08\%$ (and below 0.06% if the fluctuation frequencies below 20 Hz are filtered out).[39]

B. Plate and porous TE geometry

An elliptical-leading edge plate constructed of solid polypropylene was designed as a base structure for the porous TEs. The elliptical-leading edge has a major radius of 40 mm and a minor radius of 25 mm, as depicted in Figs. 2(a)–2(c). The chord of the plate is 350 mm, it is 25 mm thick, and its span is 400 mm to fill the test section width of the A-tunnel. The elliptical leading edge of the plate has a similar design to those in other porous TE studies[7,23] and other blunt TE noise reduction studies.[40,41]

A zig-zag tape is attached approximately 10% of the chord downstream of the elliptical leading edge to ensure that the boundary layer at the porous TE interface is turbulent for all TEs investigated, consistent with other studies.[6,42] The trip is identical to a triangular Glasfaser-Flugzeug-Service turbulator (Glasfaser-Flugzeug-Service GmbH, Grabenstetten, Germany) with a thickness of 0.5 mm, width of 6 mm, and an angle of 70° between the teeth. The benchmark study of Luesutthiviboon *et al.*[43] provides a comprehensive study of the influence this zig-zag trip on airfoil geometries in the A-tunnel, thereby avoiding the need for hot-wire anemometry and/or PIV to determine the characteristics of the boundary layer in this study.

In this study three porous TEs are investigated: the SPTE and two porous open-cell polyurethane TEs with 10 PPI (named PPI10) and 30 PPI (named PPI30). Each TE has a span of 385 mm and a thickness of $h = 25$ mm to match the plate dimensions and a streamwise length of $l = 40$ mm (i.e., $l/h = 1.6$). The remaining 15 mm of the TE across the

solid TE of 400 mm span is achieved using a small-solid section. The porous TEs are attached to the solid plate using adhesive tape at the common surface of the solid and porous TE. The PPI10 and PPI30 porous polyurethane materials were cut from a large piece of porous polyurethane foam that was also used in a previous study of porous coated cylinders[44] and have void-to-solid porosity values of 95% and 80%, respectively. The SPTE was manufactured by resin-based 3D printing. It possesses a self-repeating structure that is generated by replicating a C-shaped chip in all directions, as depicted in Figs. 2(c) and 2(d); refer to Ref. 29 for a comprehensive explanation of structured porous media design. The porosity of the SPTE can be modified by adjusting the parameters c, which have same dimensions as the SPCC,[29] being $c_1 = 1.1$ mm, $c_2 = 3.4$ mm, $c_3 = 1.75$ mm, and $c_4 = 1$ mm, leading to a void-to-solid porosity of 87% (which is intentionally between the porosity values of the PPI10 and PPI30 materials).

C. Experimental setup

A phased microphone array was installed in the anechoic plenum outside of the jet flow to measure the acoustic far-field pressure signals. The acoustic far-field pressure data were obtained using G.R.A.S. 40PH analog free-field microphones (G.R.A.S., Holte, Denmark) with integrated constant current power amplifiers, that provide a flat frequency response within ±1 dB from 50 Hz to 5 kHz and within ±2 dB from 5 to 20 kHz. The microphone distribution follows an optimized multi-arm spiral arrangement,[45] with seven spiral arms with 9 microphones each, and an additional microphone located at the center of the array, giving a total of 64 microphones. The array plane is located $z = 1.27$ m away from the plane of the plate, and the center microphone is located at $(x, y, z) = (0, 0, 0)$, which corresponds to 0.11 m above the TE of the baseline flat plate (or 0.07 m from the porous TE extension), as depicted in Fig. 3. The approximate outer dimensions of the microphone array in the x and z directions are 2 m × 1 m, respectively, to improve spatial resolution in the streamwise direction.

The data acquisition system (DAS) consisted of four National Instruments (NI) PXIe-4499 sound and vibration modules with a 24 bit resolution and 204.8 kHz maximum sampling rate (NI, Austin, TX, USA). The boards are controlled by a NI RMC-8354 computer via a NI PXIe-8370 board. Each microphone is connected to the DAS by a 10-m-long G.R.A.S. AA0028 SMB-BNC coaxial cable. The array was calibrated in amplitude and phase following the guidelines by Mueller,[46] using a G.R.A.S. 42AA pistonphone (250 Hz, 114 dB reference). For each measurement, a recording time of 16 s with a sampling frequency of 51 200 Hz was employed. For acoustic imaging purposes, the acoustic data were averaged in time blocks of 4096 samples (i.e., a time duration of 80 ms, which provides a frequency resolution of 12.5 Hz) and windowed using a Hanning weighting function with 50% data overlap following Welch's method.[47]

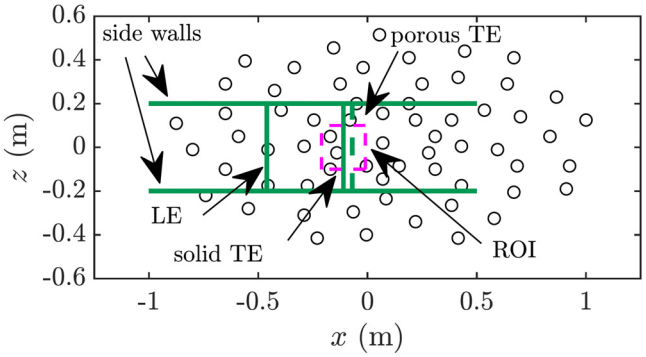

FIG. 3. (Color online) Microphone array with 64 channels and experimental setup used for acoustic measurements. A region of integration (ROI) covering the middle part of the TE of the flat plate ranging from $x = -0.1$ m to $x = 0.1$ m and from $y = -0.21$ m to $y = -0.01$ m is depicted by the dashed magenta square.

Conventional frequency domain beamforming (CFDBF) was conducted over a scanning grid ranging from $x = -0.5$ m to $x = 0.5$ m and from $y = -0.7$ m to $y = 0.3$ m with a 10 mm grid point spacing, yielding 10 201 grid points. To alleviate some of the influence of the array's geometry and aperture on the array's point spread function (PSF) from the output of CFDBF, the deconvolution approach for the mapping of acoustic sources (DAMAS)[48] was applied using 5000 iterations over a coarser grid (961 points) ranging from $x = -0.3$ m to $x = 0.3$ m and from $y = -0.6$ m to $y = 0$ m. To quantify the sound emissions by spatially distributed sources, such as TEs, integration techniques exist to reduce the influence of the array's PSF, such as the source power integration (SPI) technique and its variants.[49,50] These are typically applied to extract the sound emissions within the region of integration (ROI) under analysis. This ROI is expected to capture the main noise emissions of both flat plate configurations (e.g., baseline and porous extension) and to avoid including the typical corner sources due to the interaction between the boundary layer of the support side plates at the junction with the flat plate.[49,50] The integrated acoustic far-field spectra were integrated within the ROI for each TE configuration using the SPI method, following the guidelines in Ref. 50. The comparison with the integrated DAMAS values, however, was very similar for most of the frequency range.

III. RESULTS

Acoustic source maps are first presented and discussed in Sec. III A to reveal the acoustic source distribution of each TE configuration. Then acoustic spectra are presented in Sec. III B using only the acoustic power integrated within the ROI to remove any extraneous noise sources from the presented spectra and subsequent sound pressure level calculations. An analysis of the far-field acoustic pressure signals is conducted to reveal the acoustic directivity of each TE and coherence between three microphones within the array, and a wavelet analysis is conducted to explain the differences in periodic vortex shedding processes of each TE.

https://doi.org/10.1121/10.0028189

Prior to a detailed investigation of the specific far-field acoustic spectral characteristics and acoustic beamforming, an example spectrum recorded at $U_0 = 30$ m/s of each TE, recorded at a microphone near the array center, is presented in Fig. 4. The solid TE presents a typical vortex shedding tone of a blunt TE, and each of the porous TEs yields some tonal noise reduction. In addition, each porous TE generates some higher-frequency noise. Due to the complex noise reduction and tonal noise characteristics of each porous TE, and independent noise-generating mechanisms at higher frequencies, the acoustic spectra presented herein are extracted from a ROI via acoustic beamforming methods and the two frequency bands are discussed independently.

A. Acoustic source location

In Fig. 5, acoustic beamforming maps of each TE configuration using CFDBF at $U_0 = 30$ m/s and a one-third-octave band centered at $f = 4000$ Hz are presented. This center frequency corresponds to $St_h = 3.33$, where $St_h = fh/U_0$, which is the Strouhal number based on the TE thickness, h. Acoustic source maps obtained at this frequency band are indicative of source maps for one-third-octave bands between $f = 2000$ Hz and 8000 Hz, and in order to discuss the broadband noise generation, for brevity, only $f = 4000$ Hz is presented here. As shown in Fig. 5(a) the solid TE reveals a distributed acoustic source along the entire span of the TE, with a peak amplitude of approximately 40 dB. The acoustic sources observed at the TE are due to acoustic scattering of a blunt TE, consistent with literature.[10,23,38] This source map also reveals acoustic sources at the junctions of the leading edge and the wind tunnel side walls, around $x = \pm 0.2$ m and $y = -0.4$ m. These are typical corner sources that appear due to the interaction between the elliptical-leading-edge plate with the boundary layer that develops on the side plates. It should be noted that in order to quantify and isolate the TE noise, a ROI around the TE is considered (see Fig. 3) and the acoustic sources within this region are integrated to re-create the acoustic spectra presented in Sec. III B.

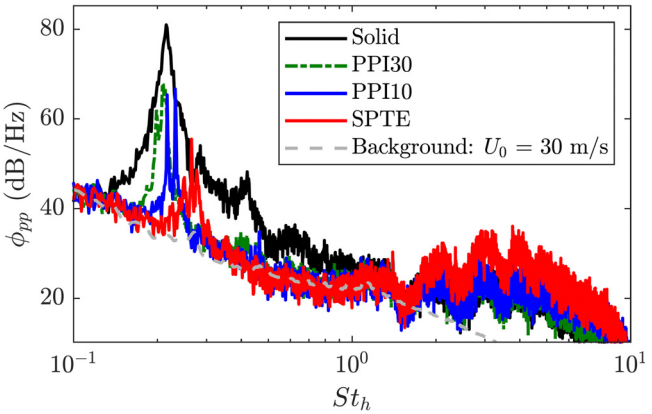

FIG. 4. (Color online) Acoustic far-field spectra, ϕ_{pp} (dB/Hz), of each TE at $U_0 = 30$ m/s.

The interaction of the TBL and the surface roughness of the PPI10 porous polyurethane causes an increased broadband contribution (relative to the smooth solid plate) and peak amplitude of 46 dB, as seen in Fig. 5(b). Similarly, as with the solid TE, acoustic sources at the intersections of the leading edge and the wind tunnel side walls are also observed. When the PPI30 material is appended to the TE, an asymmetric source distribution about the x axis is observed along the span of the TE, with a peak amplitude of 45 dB. The SPTE reveals the strongest acoustic source distribution of any TE configuration (55 dB) for this frequency band, as observed by comparing Fig. 5(d) with Figs. 5(a)–5(c). The increased peak amplitude of the SPTE is consistent with the single-microphone far-field results presented in Fig. 4. It should be mentioned that the SPTE investigated by Liu *et al.*[23] also revealed strong broadband contributions in a similar Reynolds number flow. Arcondoulis *et al.*[29] claimed that these high-frequency contributions are related to cavity modes within the porous structure of an SPCC, and Liu *et al.*[23] presented some calculations using Rossiter's formula[51] with a reasonable agreement to validate this claim for the SPTE. In addition, the increased broadband contribution of the SPTE, relative to the other porous TEs, can be conclusively determined to be located within the porous structure, as there are no other significant noise sources other than the TE noise in Fig. 5(d) to explain the differences in far-field spectra.

DAMAS was applied to each source map in Fig. 5 to generate the source maps presented in Fig. 6 that are calculated over a one-third-octave frequency band centered at $f = 4000$ Hz (corresponding to $St_h = 3.33$). Consistent with Fig. 5(a), the solid TE presents a distributed source along the TE (at $x = -0.1$), as shown in Fig. 6(a). The PPI10 configuration, in some instances, reveals more localized source distributions along the solid TE (at $x = -0.1$), as presented

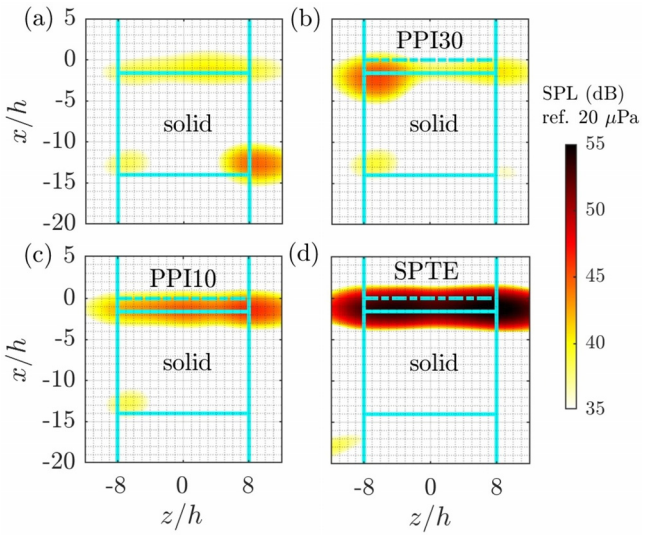

FIG. 5. (Color online) Acoustic beamforming maps of each TE configuration using CFDBF at $U_0 = 30$ m/s and a one-third-octave band centered at $f = 4000$ Hz ($St_h = 3.33$). (a) Solid, (b) PPI30, (c) PPI10, and (d) SPTE. Flow is from bottom to top.

in Fig. 6(b). This reveals evidence of smaller-scale coherent structures, relative to the solid TE case, due to the inclusion of porous media, and this also suggests the presence of an effect of the porous media in the modification of the more efficient radiation or vortical scales of a size proportional to the material porosity. These shortened scales also indicate a significant decrease in the spanwise correlation length at the TE due to porous media, also observed by others.[7,17] These smaller structures were also observed for PPI30, as shown in Fig. 6(c). PPI30 indicates that fewer acoustic sources are scattered about the TE at this frequency, and other extraneous sources dominate the evaluation of the DAMAS source map [as revealed in the CFDBF map in Fig. 5(c)]. Consistent with the CFDBF map in Fig. 5(d), the SPTE possesses the strongest acoustic sources along the TE. From Figs. 6(a)–6(c), and due to the significant improvement in spatial source resolution provided by DAMAS, it can be clearly seen that the broadband noise-generating sources of the porous cases are located within the porous media due to the interaction of the TBL and sharp solid TE (at the interface of solid-to-porous media). The SPTE spanwise source distribution is not as separated as the PPI10 and PPI30 configurations, which may indicate that the spanwise correlation length of the SPTE is less diminished by the application of porous media than the randomized porous media; future work should be considered to validate this claim. Nonetheless, for this particular frequency case, the SPTE results present consistently higher SPL values with respect to the solid baseline, reaching differences up to 15 dB.

B. Far-field spectra

1. Vortex shedding noise

The integrated acoustic far-field spectra within the ROI for each TE configuration, ϕ_{pp} (dB/Hz), of each TE over a range of flow velocities, $U_0 = 10$ to 35 m/s, are presented in Fig. 7. Note that the x axes in the plotted data are restricted to $St_h = 0.1$ to 0.5 to focus on the vortex shedding tone contributions. The solid TE reveals a strong vortex shedding tone for all considered flow velocities, as presented in Fig. 7(a). The tonal contribution, based on a 30 dB peak prominence, has a bandwidth of $St_h \approx 0.1$. The Strouhal number of the peak tonal amplitude is observed to slightly increase with U_0, which was previously observed by Ausoni *et al.*[52] in an investigation of a tripped-boundary layer hydrofoil with a blunt TE. By observation of Figs. 7(b)–7(d), each of the porous TEs shows significant noise reduction relative to the solid TE, yet they each possess unique far-field pressure spectral characteristics. The evolution of the Strouhal number of each TE type with respect to freestream velocity is presented in Fig. 8 to support the discussion of the spectral characteristics.

The PPI30 tonal noise spectrum presented in Fig. 7(b) reveals the smallest tonal noise reduction of the porous TEs for all investigated flow velocities. For $U_0 \leq 25$ m/s, a single tone is observed at $St_h \approx 0.20$ to 0.22, and at $U_0 \geq 30$ m/s, a weak secondary tone is recorded that is superimposed at a slightly lower Strouhal number, $St_h \approx 0.20$. The tonal noise recorded from PPI10, as presented in Fig. 7(c), reveals multi-tone spectral content emerging at $U_0 \geq 25$ m/s. At the lowest considered freestream velocity of $U_0 = 10$ m/s, a weak vortex shedding tone is observed at $St_h \approx 0.21$, and with increasing velocity, this tone is seen to increase in amplitude and gradually increase in St_h up to $U_0 = 20$ m/s. At $U_0 = 25$ m/s, a weaker secondary tone at a lower frequency is observed (see also Fig. 8), centered about $St_h \approx 0.215$, in a similar manner to the SPTE in Fig. 7(d). With an increased velocity, however, at $U_0 = 30$ m/s, this secondary lower-frequency tone increases in amplitude to within 2 dB of the shedding tone at $St_h \approx 0.23$, and within 3 dB at $U_0 = 35$ m/s. In order to generate two tones with similar amplitudes and Strouhal numbers, it is suggested that the vortex shedding processes of the upper and lower surfaces occur independently. One shear layer may shed

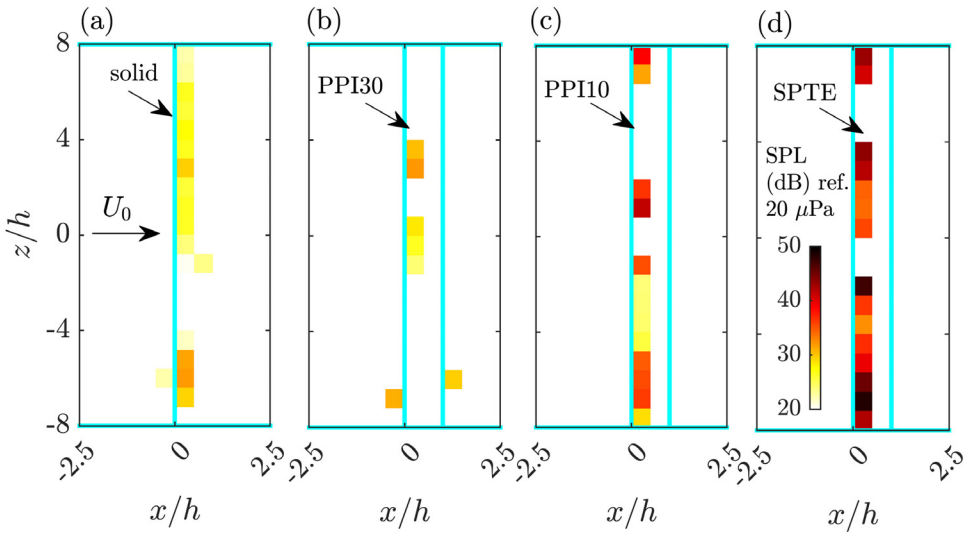

FIG. 6. (Color online) Acoustic beamforming maps of each TE configuration using DAMAS at $U_0 = 30$ m/s and a one-third-octave band centered at $f = 4000$ Hz ($St_h = 3.33$). (a) Solid, (b) PPI30, (c) PPI10, and (d) SPTE. Flow is from left to right.

https://doi.org/10.1121/10.0028189

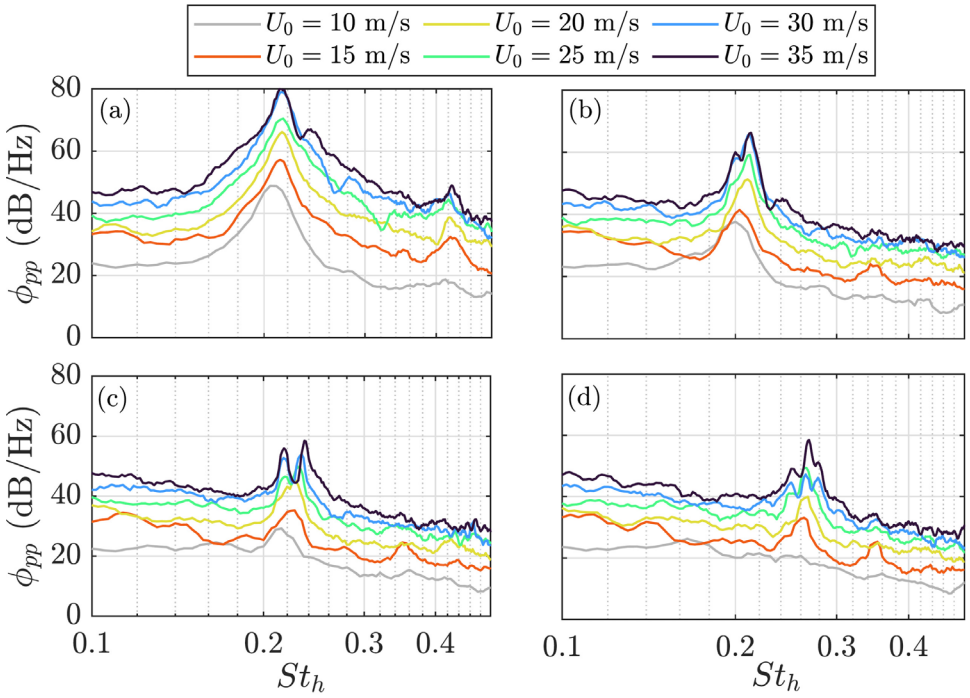

FIG. 7. (Color online) Acoustic far-field spectra, ϕ_{pp} (dB/Hz), of each TE over a range of flow velocities, $U_0 = 10$ to 35 m/s, focusing on the vortex shedding tone contribution. (a) Solid, (b) PPI30, (c) PPI10, and (d) SPTE.

closer to the TE base than the other, such that the vortex shedding generated from each shear layer occurs with different periods. Note that the peak tonal amplitudes of the SPTE and PPI10 TEs at $U_0 = 35$ m/s are similar ($\phi_{pp}|_{\max} \approx 58$ dB); however, the total tonal noise contribution of PPI10 is greater than that of the SPTE due to the inclusion of the secondary tone.

In Fig. 7(d), the SPTE is observed to typically possess a vortex shedding tone about $St_h \approx 0.26$ to 0.27 from $U_0 = 15$ m/s to 20 m/s. At $U_0 = 25$ m/s, a weaker secondary tone at a lower frequency is observed to form, centered about $St_h \approx 0.25$, and with further increases of velocity to $U_0 \geq 30$ m/s, a third tone is observed at a higher frequency, centered about $St_h \approx 0.28$, as also indicated in Fig. 8. An

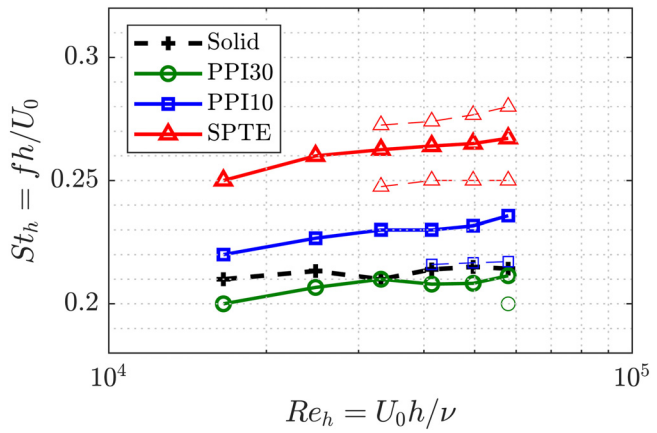

FIG. 8. (Color online) Strouhal number, St_h, dependency on TE thickness Reynolds number, Re_h. Solid lines represent the main vortex shedding tone, and the dashed lines and separate data points represent secondary tones.

interesting phenomenon occurs between $U_0 = 25$ m/s to 30 m/s, where the peak tonal amplitude is observed to decrease, yet the total tonal contribution (if integrated across $St_h \approx 0.23$ to 0.30) is seen to increase via the contribution of two additional tones, spaced about a dominant central tone at $St_h \approx 0.26$. Other published acoustic spectra of SPTEs do not reveal this multiple tone behavior,[23] which may be due to the difference in l/h-values ($l/h = 1.6$ in this study and $l/h = 3.15$ in Ref. 23). It is plausible that an extended porous plate attached to the solid TE attenuates the development of smaller-scale vortex shedding structures that are responsible for the production of multiple tones.

2. High-frequency noise

The higher-frequency noise contributions of each TE are presented in Fig. 9, where it is clear that the porous TE configurations present higher noise levels at high frequencies, as shown in the acoustic source maps of Figs. 5 and 6 and which is consistent with others.[23] This is especially the case for SPTE and $f > 3000$ Hz, where the noise increase with respect to the solid TE baseline can reach values up to 20 dB for certain frequencies. In previous studies of porous coated cylinders, an SPCC was observed to possess much stronger broadband contributions relative to their open-cell randomized porous media counterparts, even with comparable porosity and PPI,[29] as explained by local cavity resonances due to the regular spacing of the pores relative to the incoming flow field. The SPCC high-frequency content (named the HF-Band in Refs. 29 and 53) was shown to follow a Strouhal number relationship; however, the center frequencies of the broadband humps observed in the acoustic

spectra of the porous TEs are clearly shown to be independent of the freestream velocity. The case of the SPTE differs from the SPCC, in that the SPCC is subject to a flow field with a substantial normal component relative to the porous media,[33] yet the SPTE experiences tangential flow fields driven by a TBL. Thus, the tangential flow field must result in weaker acoustic noise sources due to local interaction with the structural members. This claim is made by recognizing the relatively small differences in acoustic spectral amplitudes between the SPTE and the randomized porous TEs, as compared to the significant differences in the HF-Band amplitudes of the SPCC compared to a randomized porous coated cylinder.

3. Overall sound pressure level

Figure 10 presents the acoustic far-field noise of each TE in terms of tonal, broadband, and overall contributions. The quantity $\phi_{pp|\max}$ represents the peak tonal amplitude. To estimate the total broadband contribution, the entire tone is first extracted following the criteria suggested by Aures (see Ref. 54) commonly used in the tonality metric for psychoacoustics, where the tonal component is defined as the SPL integrated around a tone considering a threshold of 7 dB under its peak. $\mathrm{SPL}|_{\mathrm{B}}$ is then the remainder broadband contribution: that is, the total overall sound pressure level (OSPL) minus excluding the tonal component. The OSPL is simply the total OSPL (including both tonal and broadband components) across 200 Hz to 10 kHz. The peak tonal magnitude presented in Fig. 10(a) reveals a clear trend of increasing tonal amplitude with increasing freestream flow speed for the solid TE. Note that the tonal contribution of each TE was extracted from the rest of the spectra following the criteria suggested by Aures,[54] so that the broadband contribution in Fig. 10(b) was defined as the remainder of the spectra, and the OSPL in Fig. 10(c) is the combination of both. In general, the porous TEs provide large tonal noise reductions (more than 20 dB) with respect to the solid TE baseline throughout the whole flow velocity range considered. In some cases of the porous TEs, local minima are observed (e.g., PPI30 at 15 m/s and SPTE at 30 m/s), yet typically the maximum tonal noise reductions are observed for the SPTE configuration. The reductions of broadband noise, on the other hand, are not as large as for the tonal counterpart (partly explained by the high-frequency broadband noise increase discussed in Fig. 9). In this case, SPTE presents lower noise reductions compared to the PPI10 and PPI30 cases. The combination of both reductions is reflected in the considerable OSPL reduction (up to 25 dB), especially for flow velocities higher than 20 m/s. Overall, the SPTE configuration provides the largest OSPL reductions, followed by PPI10 and PPI30.

C. Spatial coherence

The magnitude-squared coherence values, γ^2, between microphones in the array were calculated to investigate frequency-dependent relationships between the recorded acoustic signals[55] of each TE. Due to the huge number of microphone pair permutations in a 64-channel array, only three key microphones were selected for coherence analysis. Microphones are selected at near the array center for the peak of the dipole-shaped lobe (microphone I), a microphone upstream of the TE is selected to investigate part of the cardioid (microphone II), and a microphone aligned with the TE in the x-direction but furthest in the spanwise

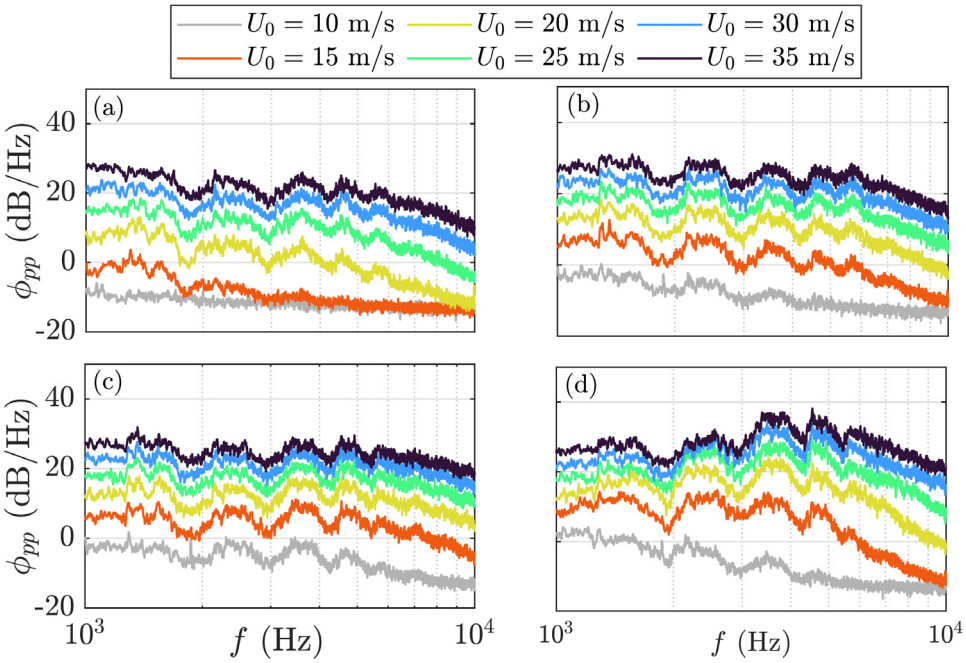

FIG. 9. (Color online) Acoustic far-field spectra, ϕ_{pp} (dB/Hz), of each TE over a range of flow velocities, $U_0 = 10$ to 35 m/s, focusing on the high-frequency broadband contribution. (a) Solid, (b) PPI30, (c) PPI10, and (d) SPTE.

https://doi.org/10.1121/10.0028189

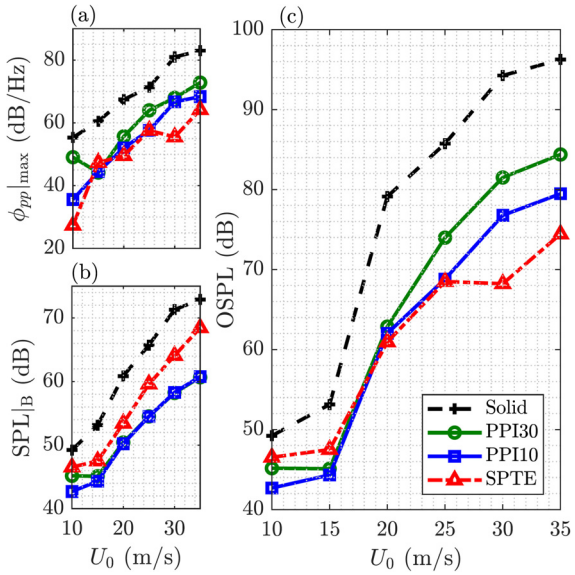

FIG. 10. (Color online) Acoustic far-field noise of each TE. (a) Peak tonal magnitude tonal contributions $\phi_{pp}|_{\max}$ (dB/Hz), (b) broadband contributions SPL$|_B$ (dB), and (c) OSPL (dB).

direction (microphone III) is chosen to investigate any spanwise effects relative to microphones I and II. The coordinates of microphones I, II, and III are identified in Fig. 11.

Figures 11(a)–11(c) present the magnitude-squared coherence between the microphone pairs I and II, II and III, and I and III, respectively. In Fig. 11(a), strong coherence is observed at $St_h \approx 0.2$ corresponding to the vortex shedding frequencies. However, each of the TEs shows a more narrow-band coherence with respect to Strouhal number, compared to the solid TE. In addition, the peak coherence amplitude within the vortex shedding frequency range appears related to the noise reduction of the TE (i.e., $\phi_{pp}|_{f_1} \sim 1/\gamma^2$). At higher Strouhal numbers between $St_h \approx 1$ to 10, the SPTE shows strong coherence between microphones I and II than the other TEs, revealing that the high-frequency contribution of the SPTE convects stronger pressure fluctuations further upstream than the other TEs. By comparing the coherence spectra between microphones II and III [in Fig. 11(b)] with Fig. 11(a), the vortex shedding pressure fluctuations are typically correlated in both the upstream and spanwise directions. The high-frequency contributions of PPI10 and the SPTE, however, have negligible coherence, meaning that the high-frequency pressure fluctuations are not coherent in the spanwise direction, which is supported by the discontinuous nature of the DAMAS beamforming source maps along the TE (see Fig. 6). This is also further supported by the results in Fig. 11(c), where the coherence between microphones II and III is presented, revealing negligible changes in the high-frequency coherence. The vortex shedding frequency range, however, is typically more coherent in the spanwise direction, which is anticipated due to both microphones being located near the maximum acoustic pressure angle of the dipole directivity. Overall, these coherence results support the acoustic beamforming spanwise distribution, which is typically marred by uncertainty, and help build a link between the discontinuous acoustic beamforming maps and the loss of coherence induced by spanwise incoherent pressure fluctuations. The discontinuity of the beamforming maps confirms the noise reduction capabilities of the materials in different frequency ranges, closing the link between aerodynamic flow fluctuations and acoustic radiation.

D. Wavelet analysis

A continuous wavelet (CWT) analysis is conducted here[56] to elucidate the emergence of multiple tone behavior of the PPI10 TE and the SPTE configurations, using the Morlet mother wavelet. To assist in the comparison of each TE, the real part of the wavelet output is normalized by its maximum value and denoted by W. In Figs. 12 and 13, time t is non-dimensionalized by tU_0/h. Note that the initial time, $tU_0/h = 0$, is arbitrarily chosen for each TE configuration.

In Fig. 12, the wavelet is recorded at microphone I for the solid, PPI30, and PPI10 TEs at $U_0 = 30$ m/s. It should be noted that data presented in this figure were also calculated at microphones II and III, and negligible differences were observed between these microphone data: i.e., the wavelet data presented in Fig. 12 are indicative of the data obtained from other microphones within the array. For each TE, there are clear periodic pulses of fluctuating pressure, with duration of $\Delta tU_0/h \approx 50$. These pulses are observed at constant Strouhal numbers, corresponding to the vortex shedding tone observed in Fig. 7. These Strouhal numbers are identified with white dashed lines. Within each periodic pulse, there are alternating positive/negative pressure fluctuations, spaced apart by $\Delta tU_0/h \approx 5$. Note that $\Delta tU_0/h \equiv 1/St_h$, and therefore these spacings are $St_h \approx 0.2$, which is directly related to the vortex shedding processes of the TE. The periodic pulses of the PPI10 are more frequent than the solid and PPI30 TEs, such that each pulse of vortex shedding is typically weaker. The SPTE also exhibits this shortening of the vortex shedding pulses, as observed in Fig. 13. Due to the significant variance in recorded pressures from the SPTE, three individual wavelet diagrams are presented for microphones I, II, and III in Figs. 13(a)–13(c), respectively.

As recorded at microphone I in Fig. 13(a), pulses of vortex shedding are observed for the SPTE configuration, which vary in frequency with respect to time, unlike the solid and PPI10 and PPI30 configurations. Some consistent shedding cycles are observed, centered about $St_h = 0.26$: for example, between $tU_0/h \approx 25$ to 60 and $tU_0/h \approx 115$ to 160. However, other lower-frequency shedding pulses are recorded between $tU_0/h \approx 75$ to 120 that vary significantly in frequency with time, sweeping between $St_h \approx 0.22$ and 0.28, corresponding to the Strouhal number range, in which tones are observed for the SPTE at $U_0 = 30$ m/s in Fig. 7(d). The wavelet patterns recorded at microphones II and III, presented in Figs. 13(b) and 13(c), respectively, yield significant differences from each other. In common between microphones I and II are the times of maximum pulse

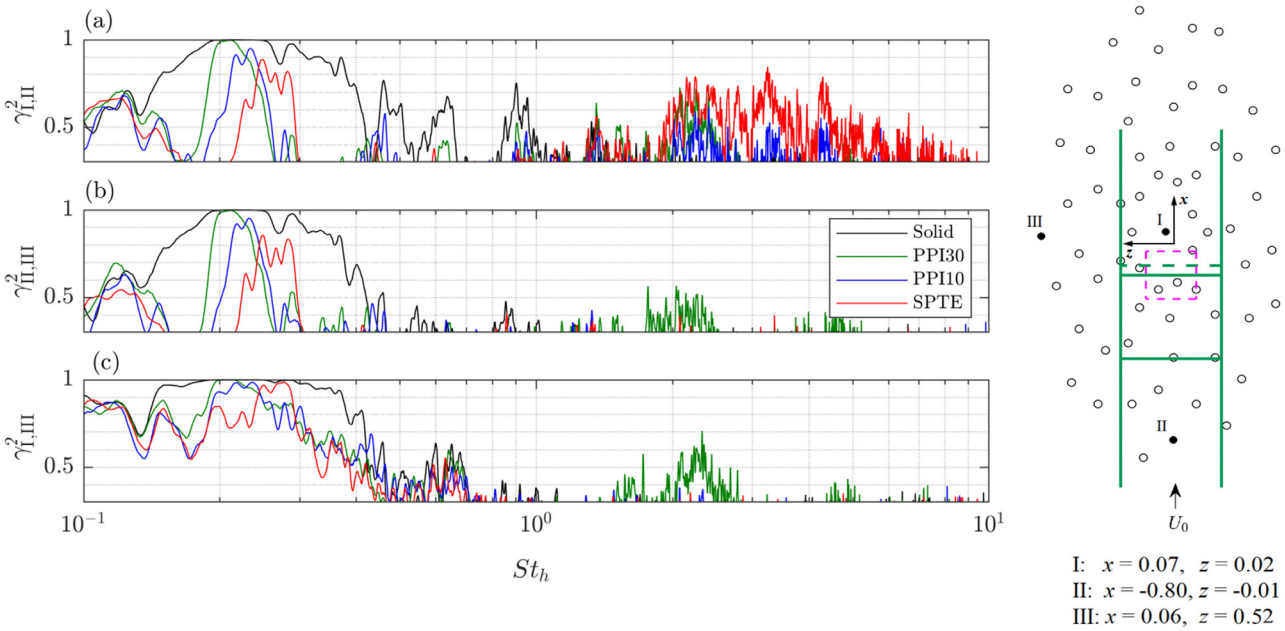

FIG. 11. (Color online) Magnitude-squared coherence, γ^2, of each TE at $U_0 = 30$ m/s between microphones (a) I and II, (b) II and III, and (c) I and III. A schematic image of the selected microphones and their coordinates within the array is included for clarity.

amplitudes, at $tU_0/h \approx 25$ to 60 and $tU_0/h \approx 115$ to 160. However, at microphone II the lower-frequency shedding pulses are not observed, and typically at microphone III, the vortex shedding spectrum is significantly weaker than that recorded by other positions within the array. This reveals evidence of the SPTE breaking down larger-scale vortex shedding structures in the near-wake, into smaller, weaker shedding structures of varying length scales that shed intermittently and with complex directionality.

IV. CONCLUSIONS

The acoustic response of several blunt porous TEs was presented, including a recently published SPTE. Experiments were conducted in an anechoic wind tunnel, where the porous TEs were appended to an elliptical-leading-edge plate that was fitted with a zig-zag trip to develop turbulent boundary layers over the TE. Acoustic beamforming revealed that, for all TEs studied, the dominant noise

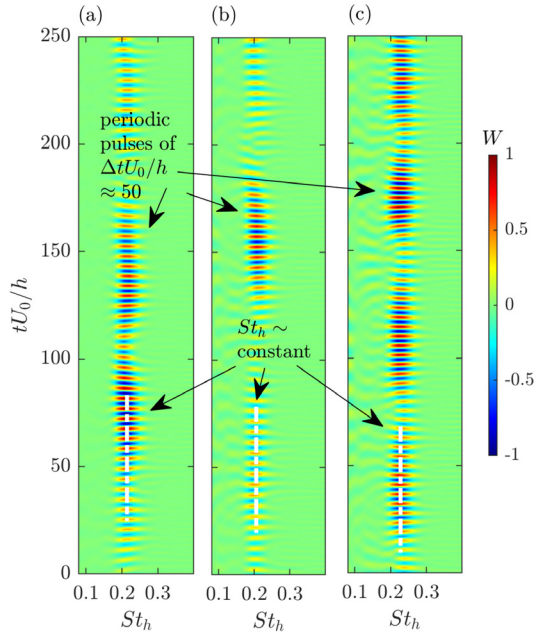

FIG. 12. (Color online) Normalized real part of the wavelet, W, at $U_0 = 30$ m/s, recorded at microphone I. (a) Solid, (b) PPI30, and (c) PPI10. The time segment is arbitrarily chosen.

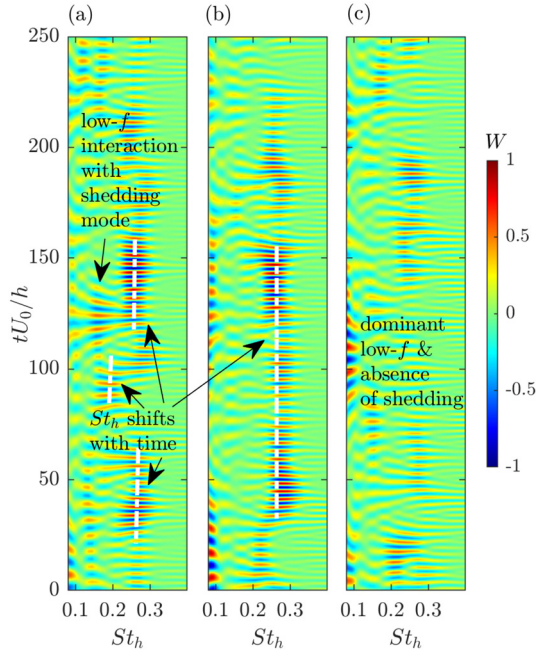

FIG. 13. (Color online) Normalized real part of the wavelet, W, of the SPTE at $U_0 = 30$ m/s, recorded at microphones (a) I, (b) II, and (c) III. The time segment is arbitrarily chosen.

https://doi.org/10.1121/10.0028189

sources are observed along the solid TE span, even when porous TEs are attached to the solid TE. To analyze and compare the acoustic far-field spectral content of each TE, a ROI was used about the mid-span of the TE. All porous TEs yielded significant noise reduction relative to the solid TE, and each TE displayed an emergence of multiple tones at flow speeds greater than 25 m/s. Porous media, when used for passive noise control, typically generate additional unwanted high-frequency noise, relative to a smooth, solid counterpart; however, in this study the high-frequency noise of these TEs was not as pronounced as a porous coated cylinder, due to the porous media being subject to predominately a tangential flow, rather than a combination of normal and tangential flow fields experienced by a cylinder. This suggests that the concept of an SPTE may be more practical from an engineering perspective, as the SPTE can be customized relative to other randomized porous media. Furthermore, this study revealed that $l/h = 1.6$ is ample to reduce the tonal noise content of the solid TE, as compared to a previous study of SPTEs that used $l/h = 3.15$. The acoustic directivity was estimated by correcting the recorded microphone pressure signals from the acoustic beamforming array to mimic a partial-ring array around the TE with radius of 1 m. The estimated acoustic directivity of each TE, solid, or porous, was typically dipolar at the peak vortex shedding frequency, consistent with noise-generating mechanisms of solid TEs. The magnitude-squared coherence between three key microphones within the array revealed that the peak coherence value of the vortex shedding frequency is inversely related to the noise reduction capability of each TE. The high-frequency noise is highly directional, and the coherence is significantly reduced between spanwise-separated measurement locations. A wavelet analysis revealed that the SPTE causes significant modification to typical periodic vortex shedding processes, by disrupting the periodic vortex shedding processes (relative to a solid or randomized porous TE) and breaking larger vortex shedding cycles into intermittent, shorter cycles across a Strouhal number range of $\Delta St_h \approx 0.06$.

From this acoustic study, it is clear that a comprehensive analysis of the flow field is needed to obtain a deeper understanding of the noise-generating mechanisms, not only of the SPTE, but also of the randomized porous TEs, and why structured porous media is capable of such disruption to the far-field noise, as compared to a randomized porous TE with similar porous properties. Future work will include a comprehensive set of flow field tests of similar porous TEs, SPTEs, via numerical and experimental methods.

ACKNOWLEDGMENTS

This research was supported by the National Natural Science Foundation of China (Grant No. 12272163).

AUTHOR DECLARATIONS

Conflict of Interest

The authors have no conflicts to disclose.

DATA AVAILABILITY

The data that support the findings of this study are available from the corresponding author upon reasonable request.

[1]T. F. Brooks, D. S. Pope, and M. A. Marcolini, "Airfoil self-noise and prediction," NASA Reference Publication 1218, NASA, Washington, DC (1989).
[2]E. Arcondoulis, C. Doolan, A. Zander, and L. Brooks, "A review of trailing edge noise generated by airfoils at low to moderate Reynolds number," Acoust. Aust. **38**(3), 129–133 (2010).
[3]T. P. Chong and P. F. Joseph, "An experimental study of airfoil instability tonal noise with trailing edge serrations," J. Sound Vib. **332**(24), 6335–6358 (2013).
[4]P. Chaitanya, P. Joseph, S. Narayanan, and J. Kim, "Aerofoil broadband noise reductions through double-wavelength leading-edge serrations: A new control concept," J. Fluid Mech. **855**, 131–151 (2018).
[5]M. B. Gelot and J. W. Kim, "Effect of serrated trailing edges on aerofoil tonal noise," J. Fluid Mech. **904**, A30 (2020).
[6]L. T. L. Pereira, F. Avallone, D. Ragni, and F. Scarano, "A parametric study of serration design for trailing-edge broadband noise reduction," Appl. Acoust. **211**, 109470 (2023).
[7]S. A. Showkat Ali, M. Azarpeyvand, and C. R. I. da Silva, "Trailing-edge flow and noise control using porous treatments," J. Fluid Mech. **850**, 83–119 (2018).
[8]S. M. Hasheminejad, T. P. Chong, G. Lacagnina, P. Joseph, J.-H. Kim, K.-S. Choi, M. Omidyeganeh, A. Pinelli, and O. Stalnov, "On the manipulation of flow and acoustic fields of a blunt trailing edge aerofoil by serrated leading edges," J. Acoust. Soc. Am. **147**(6), 3932–3947 (2020).
[9]P. B. Jonathon and C. Dam, "Drag reduction of blunt trailing-edge airfoils," in *International Colloquium on Bluff Body Aerodynamics & Applications*, Milan, Italy (2008).
[10]G. Nati, M. Kotsonis, S. Ghaemi, and F. Scarano, "Control of vortex shedding from a blunt trailing edge using plasma actuators," Exp. Therm. Fluid Sci. **46**, 199–210 (2013).
[11]J. Guo, Y. Liu, R. Maryami, and C. Yang, "Influence of base jets on trailing edge bluntness noise generation," in *AIAA AVIATION 2023 Forum*, San Diego, CA (2023), p. 4051.
[12]M. Herr, K.-S. Rossignol, J. Delfs, N. Lippitz, and M. Mößner, "Specification of porous materials for low-noise trailing-edge applications," in *20th AIAA/CEAS Aeroacoustics Conference*, Atlanta, GA (2014), p. 3041.
[13]T. F. Geyer and E. Sarradj, "Trailing edge noise of partially porous airfoils," in *20th AIAA/CEAS Aeroacoustics Conference*, Atlanta, GA (2014), p. 3039.
[14]A. Rubio Carpio, R. M. Martínez, F. Avallone, D. Ragni, M. Snellen, and S. van der Zwaag, "Experimental characterization of the turbulent boundary layer over a porous trailing edge for noise abatement," J. Sound Vib. **443**, 537–558 (2019).
[15]R. Graham, "The silent flight of owls," Aeronaut. J. **38**(286), 837–843 (1934).
[16]T. Geyer, E. Sarradj, and C. Fritzsche, "Measurement of the noise generation at the trailing edge of porous airfoils," Exp. Fluids **48**(2), 291–308 (2010).
[17]C. Teruna, F. Manegar, F. Avallone, D. Ragni, D. Casalino, and T. Carolus, "Noise reduction mechanisms of an open-cell metal-foam trailing edge," J. Fluid Mech. **898**, A18 (2020).
[18]C. Jiang, D. Moreau, C. de Silva, and C. Doolan, "Noise generation mechanisms of a micro-tube porous trailing edge," J. Sound Vib. **571**, 118085 (2024).
[19]T. F. Geyer and E. Sarradj, "Self noise reduction and aerodynamics of airfoils with porous trailing edges," Acoustics **1**(2), 393–409 (2019).
[20]Y. Bae and Y. J. Moon, "Effect of passive porous surface on the trailing-edge noise," Phys. Fluids **23**(12), 126101 (2011).
[21]S. R. Koh, M. Meinke, and W. Schröder, "Numerical analysis of the impact of permeability on trailing-edge noise," J. Sound Vib. **421**, 348–376 (2018).
[22]H. Liu, N. Chen, and Z. Hu, "Effects of non-uniform permeability on vortex shedding and noise control of blunt trailing edge," AIP Adv. **9**(8), 085018 (2019).

[23]H. Liu, Z. Hu, N. Chen, Y. Liu, and H. Fan, "Structured porous blunt trailing edge with uniform and non-uniform parameters for vortex shedding noise reduction," Appl. Acoust. **206**, 109302 (2023).
[24]M. Zhang and T. P. Chong, "Experimental investigation of the impact of porous parameters on trailing-edge noise," J. Sound Vib. **489**, 115694 (2020).
[25]C. Teruna, F. Avallone, D. Ragni, and D. Casalino, "On the noise reduction of a porous trailing edge applied to an airfoil at lifting condition," Phys. Fluids **33**(5), 055132 (2021).
[26]C. Jiang, D. Moreau, J. Fischer, and C. Doolan, "Additively manufactured sound-absorbing porous structures for airfoil trailing-edge noise control," J. Aerosp. Eng. **34**(5), 04021068 (2021).
[27]M. M. Scholz, T. Biedermann, T. P. Chong, and E. Smith, "Statistical modelling of aerofoil self-noise subjected to structured porous trailing edges," in *28th AIAA/CEAS Aeroacoustics 2022 Conference*, Southampton, UK (2022), p. 3092.
[28]C. Teruna, F. A. Manegar, F. Avallone, D. Casalino, D. Ragni, A. Rubio Carpio, and T. Carolus, "Numerical analysis of metal-foam application for trailing edge noise reduction," in *25th AIAA/CEAS Aeroacoustics Conference*, Delft, The Netherlands (2019), p. 2650.
[29]E. J. G. Arcondoulis, Y. Liu, Z. Li, Y. Yang, and Y. Wang, "Structured porous material design for passive flow and noise control of cylinders in uniform flow," Materials **12**(18), 2905 (2019).
[30]Y. Ran, Z. Deng, H. Yu, W. Chen, and D. Gao, "Review of passive control of flow past a circular cylinder," J. Vis. **26**, 1–44 (2022).
[31]E. J. G. Arcondoulis, Y. Liu, D. Ragni, F. Avallone, A. Rubio-Carpio, N. Sedaghatizadeh, Y. Yang, and Z. Li, "Internal shear layer and vortex shedding development of a structured porous coated cylinder using tomographic particle image velocimetry," J. Fluid Mech. **967**, A17 (2023).
[32]R. Maryami, E. J. Arcondoulis, Q. Liu, and Y. Liu, "Experimental near-field analysis for flow induced noise of a structured porous-coated cylinder," J. Sound Vib. **551**, 117611 (2023).
[33]M. M. Scholz, E. Arcondoulis, P. C. Woodhead, T. P. Chong, and E. Smith, "Structured porous coated cylinder modifications based on internal flow field data," in *AIAA AVIATION 2023 Forum*, San Diego, CA (2023), p. 3926.
[34]R. Maryami, E. Arcondoulis, C. Yang, M. Szoke, Z. Xiang, J. Guo, R. Wei, and Y. Liu, "Application of local blowing to a structured porous-coated cylinder for flow and noise control," in *28th AIAA/CEAS Aeroacoustics 2022 Conference*, Southampton, UK (2022), p. 2921.
[35]Z. Xu, X. Chang, H. Yu, W.-L. Chen, and D. Gao, "Structured porous surface for drag reduction and wake attenuation of cylinder flow," Ocean Eng. **247**, 110444 (2022).
[36]P. Bathla and J. Kennedy, "3D printed structured porous treatments for flow control around a circular cylinder," Fluids **5**(3), 136 (2020).
[37]H. Yu, Z. Xu, W.-L. Chen, H. Li, and D. Gao, "Attenuation of vortex street by suction through the structured porous surface," Phys. Fluids **33**(12), 125101 (2021).
[38]J. Kershner, J. Jaworski, and T. F. Geyer, "Experimental study of trailing-edge bluntness noise reduction by porous plates," in *AIAA AVIATION 2023 Forum*, San Diego, CA (2023), p. 4284.
[39]R. Merino-Martínez, A. Rubio Carpio, L. T. L. Pereira, S. van Herk, F. Avallone, D. Ragni, and M. Kotsonis, "Aeroacoustic design and characterization of the 3D-printed, open-jet, anechoic wind tunnel of Delft University of Technology," Appl. Acoust. **170**, 107504 (2020).
[40]D. J. Moreau and C. J. Doolan, "Noise-reduction mechanism of a flat-plate serrated trailing edge," AIAA J. **51**(10), 2513–2522 (2013).
[41]L. Al-Sadawi, T. P. Chong, and J.-H. Kim, "Aerodynamic noise reduction by plasma actuators for a flat plate with blunt trailing edge," J. Sound Vib. **439**, 173–193 (2019).
[42]D. Fiscaletti, L. T. L. Pereira, and D. Ragni, "Finlet rails for the reduction of the trailing-edge noise," J. Sound Vib. **568**, 118072 (2023).
[43]S. Luesutthiviboon, L. T. Lima Pereira, D. Ragni, F. Avallone, and M. Snellen, "Aeroacoustic benchmarking of trailing-edge noise from NACA 63 3–018 airfoil with trailing-edge serrations," AIAA J. **61**(1), 329–354 (2023).
[44]E. Arcondoulis and Y. Liu, "The effect of porosity on the porous coated cylinder diameter," in *Proceedings of ACOUSTICS 2018*, Adelaide, Australia (2018), pp. 1–10.
[45]S. Luesutthiviboon, A. M. Malgoezar, R. Merino-Martinez, M. Snellen, P. Sijtsma, and D. G. Simons, "Enhanced HR-CLEAN-SC for resolving multiple closely spaced sound sources," Int. J. Aeroacoust. **18**(4-5), 392–413 (2019).
[46]C. S. Allen, W. K. Blake, R. P. Dougherty, D. Lynch, P. T. Soderman, and J. R. Underbrink, *Aeroacoustic Measurements* (Springer Science & Business Media, Heidelberg, 2002).
[47]P. Welch, "The use of fast Fourier transform for the estimation of power spectra: A method based on time averaging over short, modified periodograms," IEEE Trans. Audio Electroacoust. **15**(2), 70–73 (1967).
[48]T. F. Brooks and W. M. Humphreys, "A deconvolution approach for the mapping of acoustic sources (DAMAS) determined from phased microphone arrays," J. Sound Vib. **294**(4), 856–879 (2006).
[49]R. Merino-Martínez, P. Sijtsma, M. Snellen, T. Ahlefeldt, J. Antoni, C. Bahr, D. Blacodon, D. Ernst, A. Finez, S. Funke, T. F. Geyer, S. Haxter, G. Herold, X. Huang, W. M. Humphreys, Q. Leclère, A. Malgoezar, U. Michel, T. Padois, A. Pereira, C. Picard, E. Serradj, H. Siller, D. G. Simmons, and C. Spehr, "A review of acoustic imaging methods using phased microphone arrays," CEAS Aeronaut. J. **10**(1), 197–230 (2019).
[50]R. Merino-Martínez, P. Sijtsma, A. Rubio Carpio, R. Zamponi, S. Luesutthiviboon, A. M. Malgoezar, M. Snellen, C. Schram, and D. G. Simons, "Integration methods for distributed sound sources," Int. J. Aeroacoust. **18**(4-5), 444–469 (2019).
[51]J. Rossiter, "Wind-tunnel experiments on the flow over rectangular cavities at subsonic and transonic speeds," Reports and Memoranda No. 3438, Ministry of Aviation (1964).
[52]P. Ausoni, A. Zobeiri, F. Avellan, and M. Farhat, "The effects of a tripped turbulent boundary layer on vortex shedding from a blunt trailing edge hydrofoil," J. Fluids Eng. **134**(5), 051207 (2012).
[53]E. J. G. Arcondoulis, T. F. Geyer, and Y. Liu, "An investigation of wake flows produced by asymmetrically structured porous coated cylinders," Phys. Fluids **33**(3), 037124 (2021).
[54]W. Aures, "Procedure for calculating the sensory euphony of arbitrary sound signals," Acustica **59**(2), 130–141 (1985).
[55]E. J. Arcondoulis, T. F. Geyer, and Y. Liu, "An acoustic investigation of non-uniformly structured porous coated cylinders in uniform flow," J. Acoust. Soc. Am. **150**(2), 1231–1242 (2021).
[56]M. Farge, "Wavelet transforms and their applications to turbulence," Annu. Rev. Fluid Mech. **24**(1), 395–458 (1992).